AIAA JOURNAL
Vol. 40, No. 11, November 2002

Effect of Cavitation on Vortex Dynamics in a Submerged Laminar Jet

T. Xing* and S. H. Frankel†
Purdue University, West Lafayette, Indiana 47907

The effects of cavitation on vortex dynamics in a submerged, two-dimensional, planar laminar forced jet were studied numerically. A locally homogeneous cavitation model that accounts for nonlinear bubble dynamics and bubble/bubble interactions within spherical bubble clusters was employed. The effects of varying key flow and cavitation model parameters on flow/cavitation interactions were investigated. The parameters varied include the cavitation number (vapor pressure), the bubble number density, the bubble cluster radius, and the Reynolds number. The results showed cavitation occurring in the cores of primary vortical structures when the local pressure fell below the vapor pressure. Low levels of void fraction caused significant vortex distortion, with the details depending on the model parameters. For higher Reynolds numbers and small values of the bubble cluster radius, cavitation inhibited vortex pairing and resulted in vortex splitting. All of the preceding observations were in good qualitative agreement with previous experimental and numerical studies. The vorticity transport equation was used to examine the mechanisms behind the effects of cavitation on the vortex structures, and it was found that both the dilatation and baroclinic torque terms played a role.

Nomenclature

b	=	buffer function
D	=	nozzle diameter
f_v	=	void fraction
h	=	half-width of the nozzle
N	=	number of grid points
n	=	bubble number density
P	=	Fourier transform of pressure
p	=	pressure
p_∞	=	chamber pressure
R	=	bubble radius
Re	=	Reynolds number
r	=	radius measured from jet axis
r_2	=	half-radius
$\boldsymbol{S}$	=	strain rate tensor
t	=	time
U_0	=	maximum velocity at inlet
$u_{\max}$	=	maximum velocity at measuring section
$\boldsymbol{V}$	=	velocity vector
(x, y, z)	=	Cartesian coordinate system
Δr	=	bubble cluster radius
θ	=	momentum thickness
Λ	=	constant
μ	=	molecular viscosity
ρ	=	density
σ	=	cavitation number
$\boldsymbol{\omega}$	=	vorticity
∇	=	gradient operator

Subscripts

l	=	liquid
v	=	vapor

Superscript

$*$	=	nondimensional quantity

I. Introduction

CAVITATION occurs in liquids when the local pressure drops below the saturated vapor pressure. This typically requires the presence of nucleation sites, which are usually small bubbles or air entrained within the fluid or trapped in solid crevices. In a flowing fluid, instabilities and turbulence often result in the formation of large-scale vortical structures. The pressure in the cores of these structures may fall below the local vapor pressure, providing favorable conditions for cavitation inception.[1−3] In addition, vapor formation also lowers the local density, which may have a significant effect on the local flowfield. There have been a number of recent experimental and numerical studies examining flow/cavitation interactions, which serve to motivate the present study.

Sridhar and Katz[4] examined the effect of entrained bubbles on the structure of vortex rings. Their experimental studies showed that the presence of only a few microscopic bubbles at very low void fraction can significantly affect the vortex dynamics within the impulsively started jets. When bubbles were entrained in the vortex ring, they observed a shift and distortion of the vortex core, and depending on the number of bubbles and their relative locations within the vortex, they also observed a splitting of the vortex and an intensification of the local vorticity. They explained these observations based on changes in the liquid momentum due to the presence of the vapor bubbles.

Gopalan et al.[5] conducted experimental studies of submerged water jets and showed cavitation occurring in the cores of either primary Kelvin–Helmholtz rollers or secondary streamwise vortical structures, depending on whether or not the jet was tripped at the nozzle exit. This highlights the sensitivity of jet cavitation to inlet conditions in experiments, industrial applications, or numerical simulations.

Cerutti et al.[6] compared predictions of cavitation inception rates in jets using an axisymmetric vorticity–stream function approach and a Lagrangian bubble tracking method. Results were in qualitative agreement with experimental observations of Gopalan et al.,[5] although they did not consider the effect of the bubbles on the flow. These bubble/fluid interactions were recently shown to have a significant influence on energy distributions in free-shear flows.[7]

There have been a number of papers attempting to couple computational fluid dynamics solvers to various cavitation models to study numerically some of the mentioned effects. Cavitating flows

Received 30 June 2001; revision received 21 June 2002; accepted for publication 24 June 2002.

*Doctoral Student, School of Mechanical Engineering. Student Member AIAA.

†Associate Professor, School of Mechanical Engineering; frankel@ecn.purdue.edu. Senior Member AIAA.

feature both incompressible and compressible flow behaviors due to the presence of both pure liquid in noncavitating regions and two-phase (liquid/vapor) in cavitating regions. This makes modeling such flows numerically challenging because the computer code must handle a range of Mach numbers. Preconditioning strategies have been introduced by Turkel[8] and others to enable efficient use of compressible flow codes at low Mach numbers. Recent pressure-based approaches have also been developed for modeling turbulent cavitating flows.[9] The incompressible cavitation model of Kubota et al.[10] avoids these problems. The model of Kubota et al. assumes homogeneous, isothermal, two-phase flow and accounts for the important effects of bubble dynamics by incorporating a modified version of the Rayleigh equation. The model accounts for bubble/bubble interactions within spherical bubble clusters distributed throughout the flow. The model neglects the mass and momentum of the vapor, the change of liquid mass due to phase change, and the changes in bubble number density as bubbles grow and decay. The model is only valid for low void fractions where the bubble radius is much smaller than the mean flow structures, so that bubbles are dominated by viscous effects and buoyancy effects can be neglected. The model was applied to study unsteady cavitation on a hydrofoil section and produced reasonable results. More recently, the model has been extended by Delale et al.[11] by relating the size of the bubble cluster radius to some multiple of the local bubble radius (assumed uniform throughout the cluster). When the cluster size is equal to the local bubble radius, the model reverts back to the original Rayleigh equation for a single bubble, which does not account for bubble/bubble interactions. If the cluster size is greater than the local bubble radius, then the model relates the local number of bubbles to the local void fraction. This modifies the original assumption of constant bubble number density in the Kubota et al.[10] model to one of constant bubble number per unit mass. This latter assumption is more consistent with the modeling efforts of Chen and Heister.[12] Other modeling efforts include the two-fluid modeling work of Grogger and Alajbegovic,[13] the compressible flow model of Schmidt et al.,[14] and the volume of fluid model presented by Sauer and Schnerr[15] and used in the FLUENT software.

In this work, the model of Kubota et al.,[10] henceforth referred to as Kubota's model, was employed to study cavitation in submerged planar jets. In particular, the focus was on the two-way coupling between the flow and the cavitation process. The choice of submerged planar jets was motivated by our interest in cavitation in hydraulic valves and the recent experimental evidence that such flows involve large-scale vortical structures that form as part of the unsteady turbulent jet flow.[16] In addition, several of the recent experimental studies of flow/cavitation interactions have involved free-shear flows, including jets, as already discussed.

II. Governing Equations

The following form of the Navier–Stokes equations were considered in this study:

$$\frac{\partial \rho}{\partial t} + \nabla \cdot (\rho \boldsymbol{V}) = 0 \tag{1}$$

$$\frac{\partial (\rho \boldsymbol{V})}{\partial t} + \nabla \cdot (\rho \boldsymbol{V}\boldsymbol{V}) = -\nabla p + 2\nabla \cdot (\mu \boldsymbol{S}) - \frac{2}{3}\nabla(\mu \nabla \cdot \boldsymbol{V}) \tag{2}$$

The density of the liquid/vapor bubble mixture is defined as

$$\rho = (1 - f_v)\rho_l \tag{3}$$

where ρ_l is the liquid density (the vapor density assumed to be negligible compared to the liquid density) and f_v, the local void fraction, is defined as

$$f_v = n\tfrac{4}{3}\pi R^3 \tag{4}$$

with $0 < f_v < 1$. The mixture viscosity is evaluated using

$$\mu = (1 - f_v)\mu_l + f_v \mu_v \tag{5}$$

where μ_l is the liquid viscosity and μ_v is the vapor viscosity, and both are assumed constant.

The bubble number density is assumed constant in both space and time, which limits the accuracy of the model for large void fractions by neglecting bubble coalescence and splitting. The Rayleigh equation governs the dynamic behavior of a single bubble in a quiescent medium.[3] Because grid resolution in most numerical simulations is insufficient to resolve individual bubbles, Kubota et al.[10] modified the Rayleigh equation to account for interactions between bubbles (of the same radius R), which may occur at scales below the grid scale. The final equation, referred to as the local homogeneous model (LHM) equation, is given as

$$[1 + 2\pi(\Delta r)^2 n R]R\frac{\mathrm{D}^2 R}{\mathrm{D}t^2} + \left[\frac{3}{2} + 4\pi(\Delta r)^2 n R\right]\left(\frac{\mathrm{D}R}{\mathrm{D}t}\right)^2 + 2\pi(\Delta r)^2 \frac{\mathrm{D}n}{\mathrm{D}t} R^2 \frac{\mathrm{D}R}{\mathrm{D}t} = \frac{p_v - p}{\rho_l} \tag{6}$$

where $\mathrm{D}/\mathrm{D}t$ is the material derivative, Δr is the bubble cluster radius (distance over which bubbles may interact with each other in a given cluster), and p_v is the vapor pressure of the liquid for a given temperature. Surface tension, thermal, and viscous effects have been neglected in the preceding equation. Notice that, as the bubble cluster radius goes to zero, the Rayleigh equation for a single bubble is recovered and bubble/bubble interactions are no longer included in the equation. Recently, Delale et al.[11] have revised Kubota's model and have addressed two important effects related to bubble/bubble interactions and viscous damping. In Kubota's original model, the bubble cluster radius is chosen to be the grid interval. In the work of Delale et al.,[11] they related the bubble cluster radius to the radius of the bubbles within the cluster itself (which is assumed the same for all bubbles within the cluster, but may grow or decay depending on the local pressure), as follows:

$$\Delta r = \Lambda R \tag{7}$$

where $\Lambda = \text{const} \gg 1$. (If $\Lambda = 1$, then the classical Rayleigh equation is recovered.) This model assumes that local number of bubbles within a cluster is proportional to the local volume of a bubble and, hence, the local void fraction.

To couple the LHM equation for the bubble radius to the Navier–Stokes equations, Kubota et al.[10] derived a quasi-Poisson equation for the pressure, which is given hereafter (for more details, see Ref. 10). Here,

$$\nabla^2 p + \Theta(p) = \Phi\left(\rho \boldsymbol{V}, \boldsymbol{V}, \frac{\partial R}{\partial t}, R\right) + \Omega(\rho \boldsymbol{V}, \boldsymbol{V}) \tag{8}$$

with

$$\Theta(p) = \rho_l 4n\pi R^2 \frac{p_v - p}{[1 + 2\pi(\Delta r)^2 n R]R\rho_L} \tag{9}$$

$$\Phi\left(\rho \boldsymbol{V}, \boldsymbol{V}, \frac{\partial R}{\partial t}, R\right) = -\rho_l 4n\pi R\left\{R\Psi\left(\rho \boldsymbol{V}, \boldsymbol{V}, \frac{\partial R}{\partial t}, R\right) + 2\left(\frac{\partial R}{\partial t}\right)^2\right\} \tag{10}$$

with

$$\Psi\left(\rho \boldsymbol{V}, \boldsymbol{V}, \frac{\partial R}{\partial t}, R\right) = \frac{\partial^2 R}{\partial t^2} - \Pi(p) \tag{11}$$

$$\Pi(p) = \frac{p_v - p}{[1 + 2\pi(\Delta r)^2 n R]R\rho_l} \tag{12}$$

Maximum and minimum void fractions were specified to avoid pure liquid and vapor states with $\Theta = \Phi = 0$ with the bubble radius fixed. In the present implementation, a hyperbolic tangent function was used to ensure a smooth variation between these two extreme states. All quantities and equations were nondimensionalized by the liquid density and viscosity, the jet nozzle half-width h, maximum velocity at jet inlet U_0, and dynamic pressure $\rho_l U_0^2$.

III. Numerical Method

Kubota et al.[10] integrated the preceding equations using a first-order Euler time integration with second-order central differences for spatial discretization. They had to include artificial dissipation to both the momentum and LHM equations. In this study, the momentum and LHM equations were spatially discretized using sixth-order compact central differences for interior points and a third-order compact scheme applied near or at the boundary of the computational domain.[17] The quasi-Poisson equation was discretized using second-order central differences to facilitate implementation of the line successive overrelaxation (LSOR) solver and the multigrid acceleration techniques.[18] Both fourth-order Runge–Kutta and first-order Euler time integration were considered, but the Euler time integration was chosen for computational efficiency. A fourth-order explicit compact spatial filter was applied to the flow variables after each time step to eliminate spurious high-frequency numerical errors.

IV. Problem Description

Recently, Gopalan et al.[5] studied the flow structure in the near field of submerged water jets and its effect on cavitation inception. They found that for untripped jets, cavitation inception occurred in the core of strong streamwise vortices, which formed just downstream of the nozzle exit. For tripped jets, the Kelvin–Helmholtz instability produced vortex rollup, and cavitation occurred in the cores of these, basically axisymmetric, vortical structures. Sridhar and Katz[4] studied the effect of entrained bubbles on vortex ring structure. They found that even a few bubbles at overall low void fraction could have a significant effect on the vortex ring structure. In certain instances, entrained bubbles distorted and split a single vortex into two structures and intensified the local vorticity. In our two-dimensional, planar cavitating jet simulations, we cannot simulate the untripped jet of Gopalan et al.,[5] which features strong three-dimensional flow structures early in the jet. However, we can, at least qualitatively, study the tripped jet case, which features unsteady vortex rollup and cavitation. In addition, because our cavitation model accounts for the interaction between the bubble dynamics and the flow structure, we can also study the effect of cavitation (bubbles) on vortex dynamics and make qualitative comparisons to the experiments of Sridhar and Katz.[4]

Motivated by the preceding discussion, two-dimensional simulations of a planar submerged water jet exhausting into a chamber were conducted using the cavitation model, governing equations, and numerical methods described earlier. The computational domain is shown in Fig. 1. A rectangular computational domain was chosen to represent the chamber. The jet was modeled just downstream of the nozzle by specifying a hyperbolic tangent velocity profile at the inlet with nondimensional momentum thickness of 0.32. A small amplitude sinusoidal disturbance was added to this base profile with Strouhal number of the primary frequency chosen as 0.223. The secondary frequency was half of this value. The nondimensional forcing period was 4.49. The jet Reynolds number was based on the nozzle half-width. For practical considerations regarding scaling effects, varying the Reynolds number is of interest. For the two-dimensional simulations considered here, varying the Reynolds number did not result in significant qualitative changes to the flow/cavitation interactions. To examine scaling effects associated with the Reynolds number and turbulence, experiments or three-dimensional large eddy simulations would be needed. This will be considered in future studies.

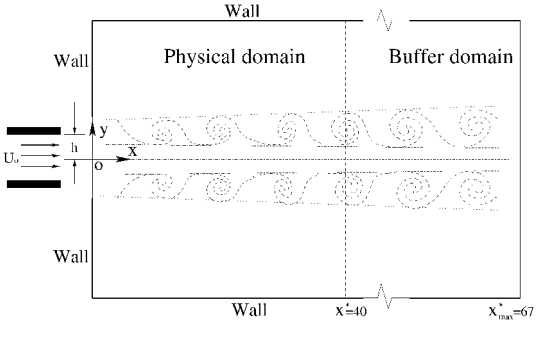

Fig. 1 Computational domain.

Table 1 Flow and cavitation model parameters for the simulation cases

Case	Re	σ	p_v	n	Δr
A	600	1.80	0.10	10^6	0.1
B	600	0.80	0.60	10^6	0.1
C	600	0.90	0.55	10^6	0.1
D	600	0.80	0.60	10^4	0.1
E	600	0.80	0.60	10^6	1.0
F	1000	1.80	0.10	10^6	0.2
G	1000	0.80	0.60	10^6	0.2

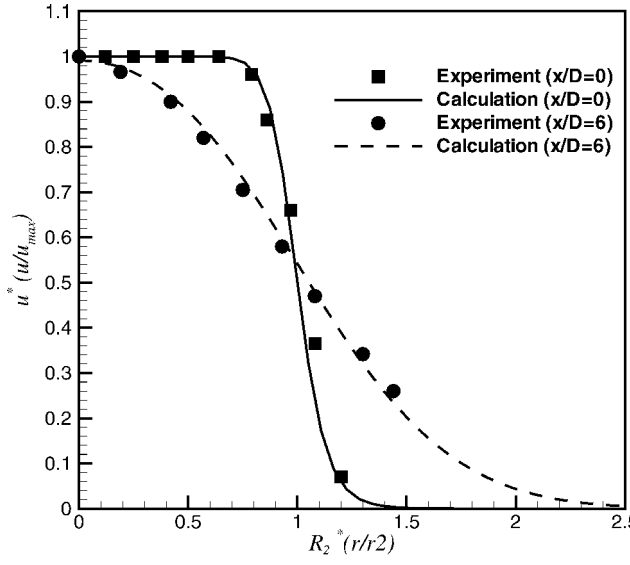

Fig. 2 Axial velocity profile in a submerged laminar jet.

Another very important parameter for cavitating flows is the cavitation number. The cavitation number was defined here in terms of dimensional quantities as $\sigma = (p_\infty - p_v)/0.5\rho_l U_0^2$. The cavitation number was varied by changing the vapor pressure. The Reynolds number was defined as $\rho_l h U_0/\mu_l$ and serves to determine the liquid viscosity. The ratio of the vapor to liquid viscosity was 0.00912 following Kubota et al.[10]

The computational domain extended from $-7.5 \le y^* \le 7.5$ in the transverse direction and $0 \le x^* \le 67$ in the streamwise direction. A nonuniform Cartesian grid with 513×129 points was employed. Grid stretching was used in the streamwise and transverse directions to facilitate resolution of the jet shear layers. Nonslip velocity boundary conditions were enforced at the top and bottom of the domain, with extrapolation for the pressure. At the outflow, a buffer domain extending from $40 \le x^* \le 67$ was employed that featured enhanced grid stretching (there were 73 points used in the axial direction in the buffer domain) and a smoothly vanishing viscosity. This resulted in a purely convective outflow condition, which tended to minimize spurious reflections.[19]

The simulation parameters considered here are presented in Table 1. Three different parameters were varied. These were the cavitation number σ (or, equivalently, the vapor pressure p_v), the bubble number density n, and the bubble cluster radius Δr. In addition, a noncavitating case at the same Reynolds number was simulated for comparison purposes by lowering the vapor pressure to a value lower than that achieved by the flow anywhere in the computational domain. The simulations were run out to a nondimensional time of $t^* = 111.8$. Statistics were gathered for comparison purposes for a time period from $t^* = 40$ to 111.8, which is equal to 16 times the main forcing period.

V. Code Validation, Grid, and Domain Effects

The computer code was validated for a noncavitating submerged laminar jet and predictions were in satisfactory agreement with the

experimental measurements of Akaike and Nemoto.[20] Predictions and measurements of axial velocity profiles are in satisfactory agreement, as shown in Fig. 2.

To assess the numerical accuracy of the simulations, a grid refinement study was conducted. In addition, the effect of the domain size was examined by varying axial location of the outflow boundary. In the grid refinement study, the number of grid points in the vertical direction was roughly doubled. Figure 3 shows a transverse profile of the instantaneous axial velocity at $x^* = 20$ from simulations with two different vertical grid sizes for case B. The two profiles are similar, suggesting adequate grid resolution. (Results were similar at other axial locations and times.) Increasing the spatial extent of the computational domain in the axial direction did not change the results. The instantaneous vorticity fields at $t^* = 44$ are identical for two calculations with different domain sizes, as shown in Fig. 4. Hence, we employed the original domain and a grid size of 513×129 for all of the results presented in the rest of the paper.

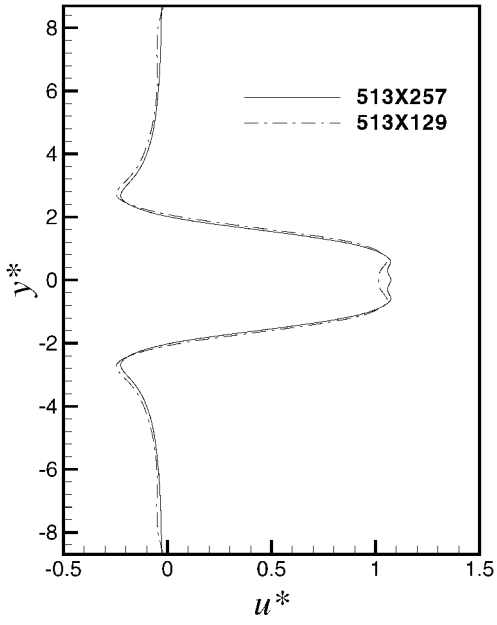

Fig. 3 Instantaneous axial velocity profiles at $t^* = 40$ for two different transverse grid sizes.

VI. Results and Discussion

A. Cavitating vs Noncavitating Jets

In this section we compare simulation results for the noncavitating case, case A, with those for the cavitating case, case B. The only difference between these two cases is the cavitation number. The overall effect of cavitation on the jet growth can be discerned from a plot of the axial variation of the momentum thickness shown in Fig. 5. Cavitation tends to suppress the jet growth in the first half of the jet in the region corresponding to $0 \le x^* \le 12$. This is followed by a rapid increase in the jet growth between $12 \le x^* \le 14$. Then the cavitating jet growth tends to level off. The location of the rapid increase in the growth of the jet at $x^* = 12$ roughly corresponds to the first location of vapor as determined from instantaneous contour plots (to be shown) and can be thought of as the location of cavitation inception. The jet growth suppression in the first half of the jet is then attributed to the decrease in density due to vapor formation stabilizing the jet. The rapid increase in jet growth downstream of this region is then related to pure expansion effects due to the presence of the vapor. This initial suppression, followed by subsequent growth due to density variations, is similar to the two-way coupling effects for the case of uniform bubble-phase concentration in a mixing layer.[21]

In Figs. 6 and 7, contour plots of instantaneous vorticity at three different times are compared for both cases. In this and all plots to follow, t^* is the nondimensional time defined as $t^* = tU_0/h$. In Fig. 6, the Kelvin–Helmholtz vortex rollup and pairing process can be clearly seen. In Fig. 7a, the plot at nondimensional time $t^* = 44$ is similar to that in Fig. 6a. At $t^* = 48$ and 52, differences in the vortical structure between the cavitating and noncavitating cases can be seen. These differences are attributed to the presence of vapor near the cores of the second pair of vortical structures at $t^* = 44$

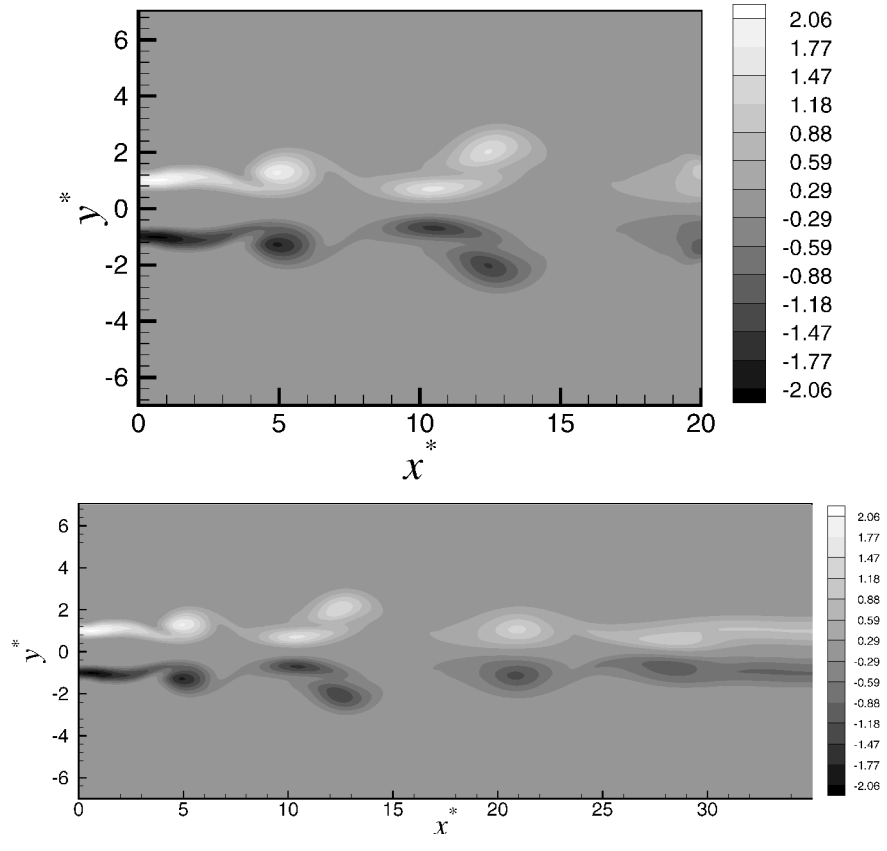

Fig. 4 Instantaneous vorticity contour plots demonstrating the influence of the streamwise size of the computational domain for case A.

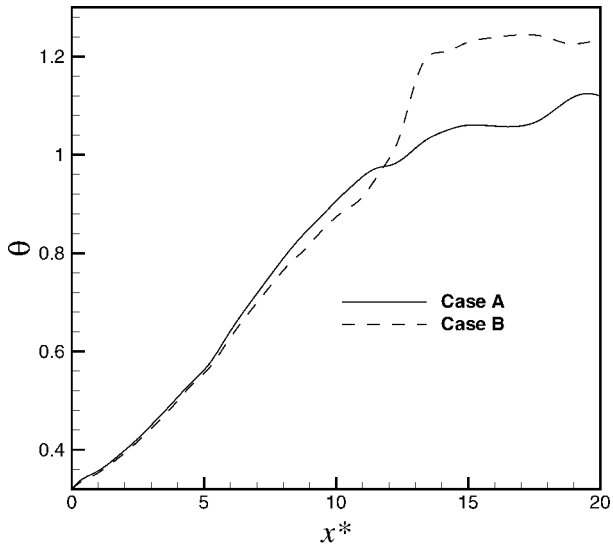

Fig. 5 Effect of cavitation on momentum thickness vs axial distance for noncavitating case A and cavitating case B.

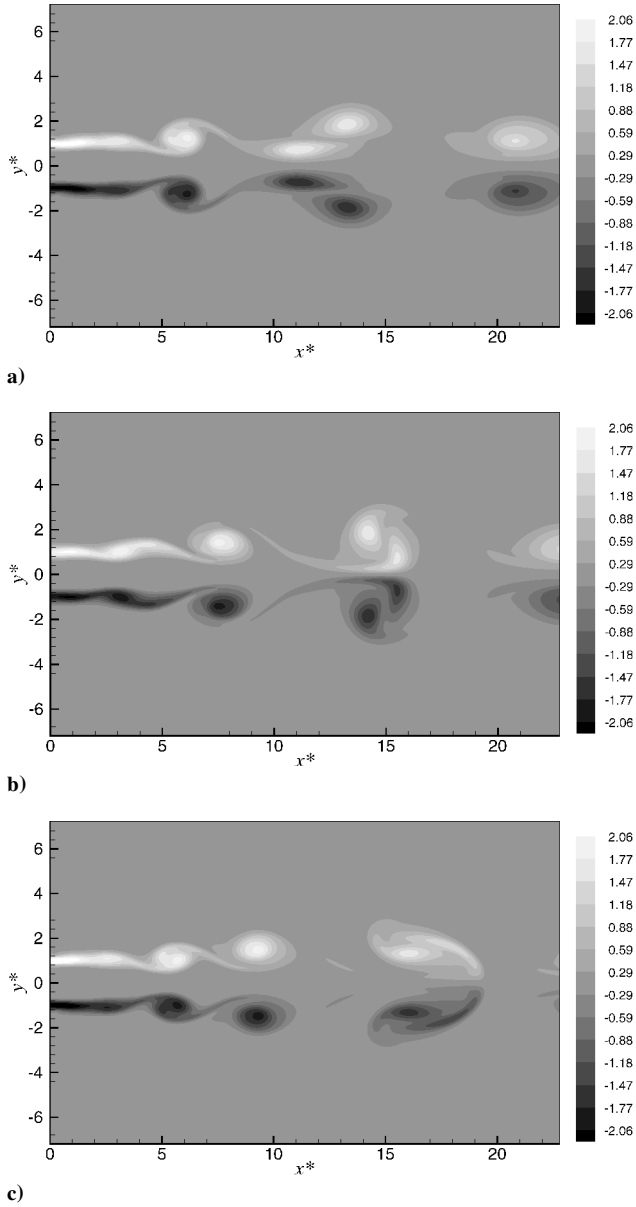

Fig. 6 Contour plots of instantaneous vorticity for the noncavitating case, case A: a) $t^* = 44$, b) $t^* = 48$, and c) $t^* = 52$.

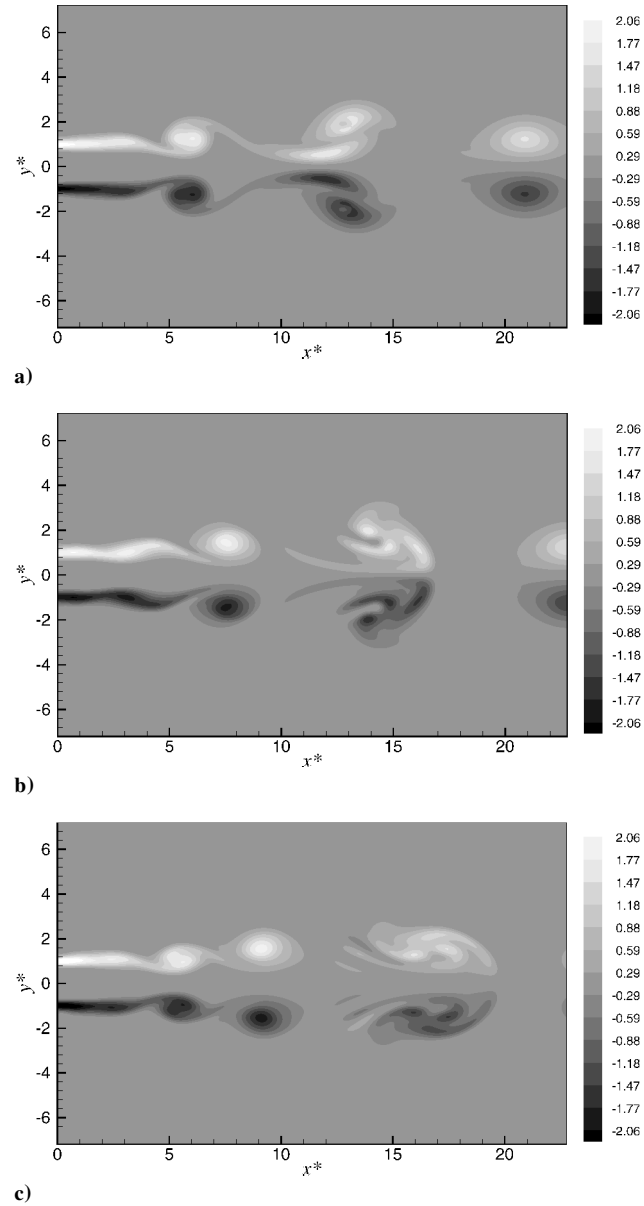

Fig. 7 Contour plots of instantaneous vorticity for cavitating case, case B: a) $t^* = 44$, b) $t^* = 48$, and c) $t^* = 52$.

in Fig. 7. To quantify these differences, closeups showing instantaneous velocity vectors, vorticity contours, and pressure contours are presented in Figs. 8 and 9 for the noncavitating and cavitating cases, respectively. Because of cavitation, the location of the primary vortex core, as indicated by the center of the rotational flow pattern in the velocity vector plots, has shifted vertically upward approximately 0.15, the core has expanded, and the velocity has decreased. Cavitation appears to have to distorted and elongated the vortical structures. These observations are all in good qualitative agreement with the experimental findings reported by Sridhar and Katz.[4] The vortex pairing process has also been inhibited by cavitation, and an additional vortex can be seen in Fig. 7b. Finally, the pressure in the core of the primary vortex is higher in the cavitating case as compared to the noncavitating case. This is because, when the local pressure falls below the vapor pressure, vapor formation in the cavitating cases serves to limit the lowest pressure within the flowfield.

To observe cavitation inception and the unsteady fluctuations associated with cavitation, a comparison between the noncavitating and cavitating cases, cases A and B, respectively, for the temporal evolution of the instantaneous pressure at a fixed point within the domain is shown in Fig. 10. The coordinates of the fixed point, $x^* = 5.78$ and $y^* = 1.75$, correspond to a location where the vortex

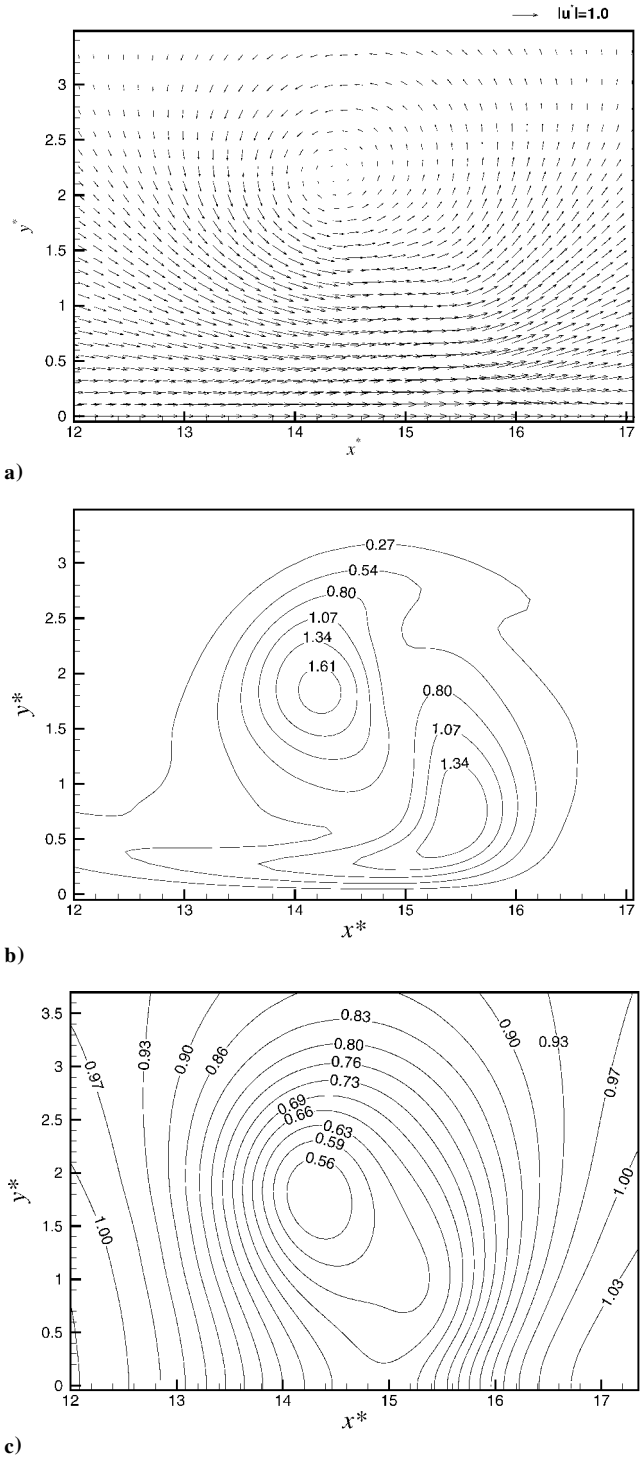

Fig. 8 Closeup of instantaneous a) velocity vectors, b) vorticity contours, and c) pressure contours at $t^* = 48$ for the noncavitating case, case A.

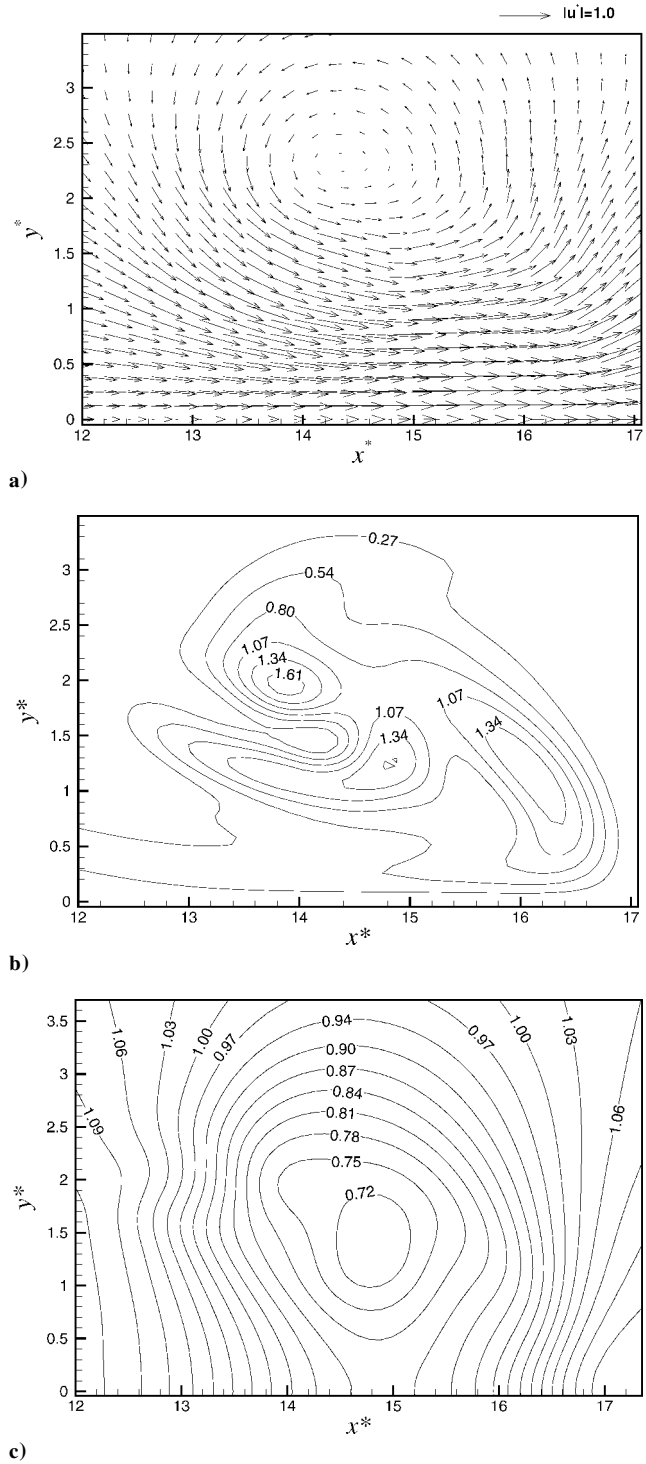

Fig. 9 Closeup of instantaneous a) velocity vectors, b) vorticity contours, and c) pressure contours at $t^* = 48$ for the cavitating case, case B.

center passes. From Fig. 10, we can see that before $t^* = 42$, cavitation has not yet occurred because the minimum pressure within the domain has not yet dropped below the specified vapor pressure. Because of the elliptical nature of the quasi-Poisson pressure equation, we can infer that there are no pressure fluctuations (hence, vapor) anywhere else in the computational domain at this time. Hence, the pressure signals between the cavitating and noncavitating cases are identical at this time. The low-frequency pressure variations in both signals are due to the passing of a vortical structure. At $t^* = 42$, cavitation inception occurs when the local flow pressure drops below the vapor pressure (not necessarily at this location). As a result, high-frequency pressure oscillations are observed to occur, which are indicative of bubble dynamics (alternative bubble growth and collapse) occurring somewhere in the domain. After $t^* = 46$, the oscillations disappear as the lowest pressure within the domain recovers above the vapor pressure. The high-frequency pressure fluctuations are caused by bubble growth and collapse inside the cavitating region. The high frequency was resolved by the current time step, as can be seen in a closeup of the region in case B shown in Fig. 11a. Sample results from Fourier analysis of the pressure signals are shown in Fig. 11b, where P is the Fourier transform of p^*. For the noncavitating case, the dominant frequency was 0.223 Hz, which corresponds to the jet forcing frequency. For the cavitating case B, two dominant frequencies can be observed. The first frequency was the forcing frequency as in the noncavitating jet, but the second was a higher frequency of 50 Hz, which

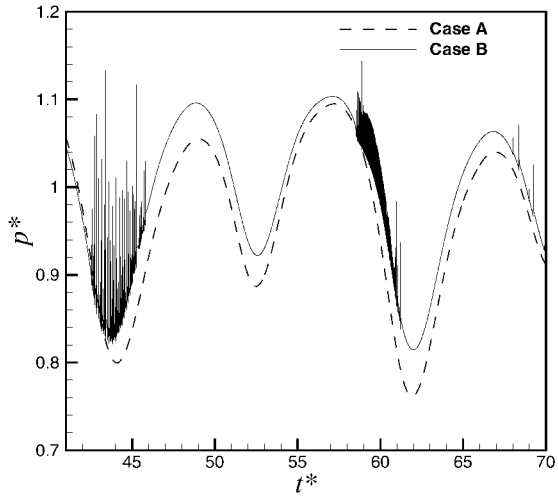

Fig. 10 Temporal evolution of instantaneous pressure at one fixed point for cases A and B.

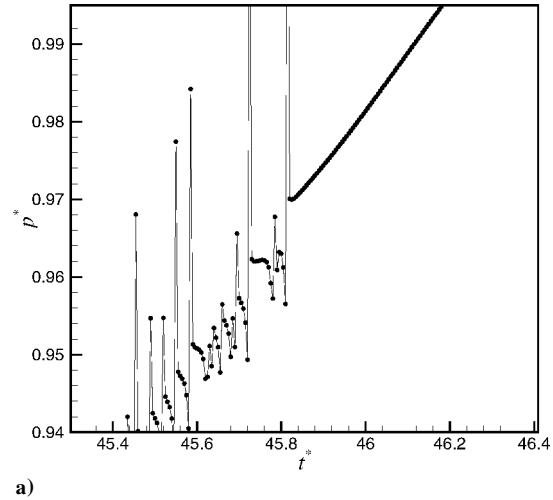

a)

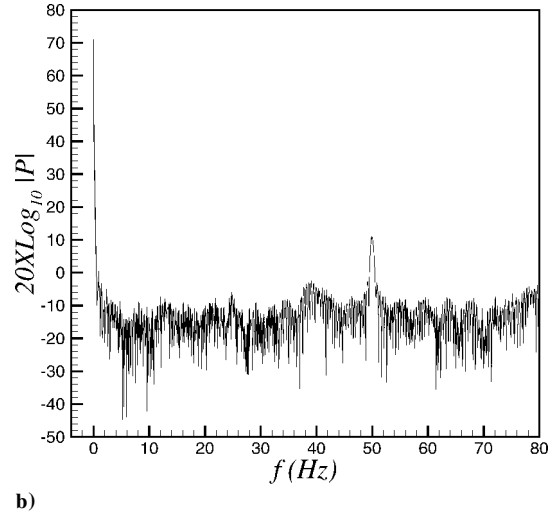

b)

Fig. 11 Further analysis of pressure fluctuations for case B showing a) closeup and b) Fourier analysis.

corresponds to the high-frequency pressure fluctuations caused by cavitation. Similar pressure oscillations can be observed in other studies.[12,22]

B. Effect of Cavitation Number

The effect of cavitation number can be studied by comparing results from cases B and C. The cavitation number was increased in case C by decreasing the vapor pressure. All other parameters were the same between the two cases. In Fig. 12, closeups of the vorticity and pressure contours for the same region as in Fig. 9 are shown. The velocity vector plots were similar for both cases and are not shown. The vorticity contours still reveal three main vortical regions, although the magnitude of the vorticity has decreased everywhere in the region shown. The pressure contours show that by lowering the vapor pressure and, hence, increasing the cavitation number, the values of the pressure have decreased everywhere in the region shown. This is because the flow is able to reach a lower pressure before cavitation inception and vapor formation occur, which tends to limit the lowest pressure as already discussed in the comparison

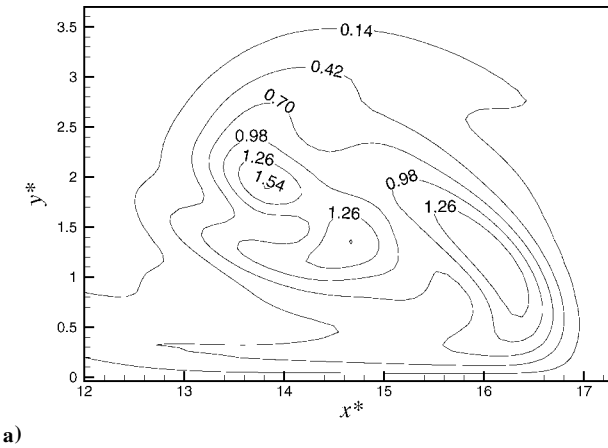

a)

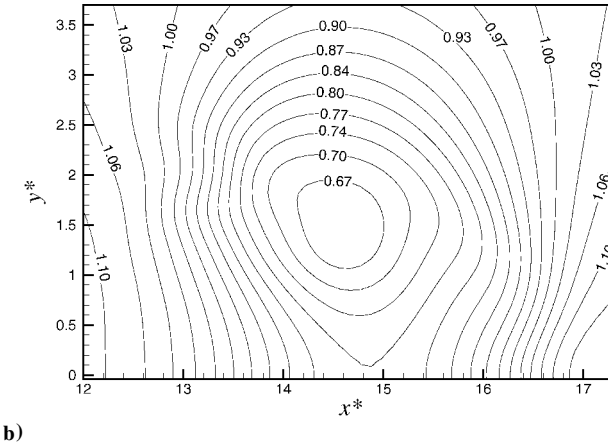

b)

Fig. 12 Closeup of instantaneous a) vorticity and b) pressure contours at $t^* = 48$ for the cavitating case, case C.

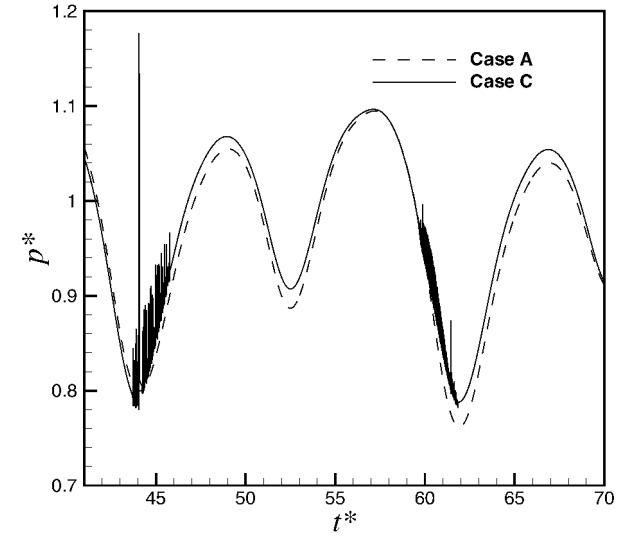

Fig. 13 Temporal evolution of instantaneous pressure at one fixed point for cases A and C.

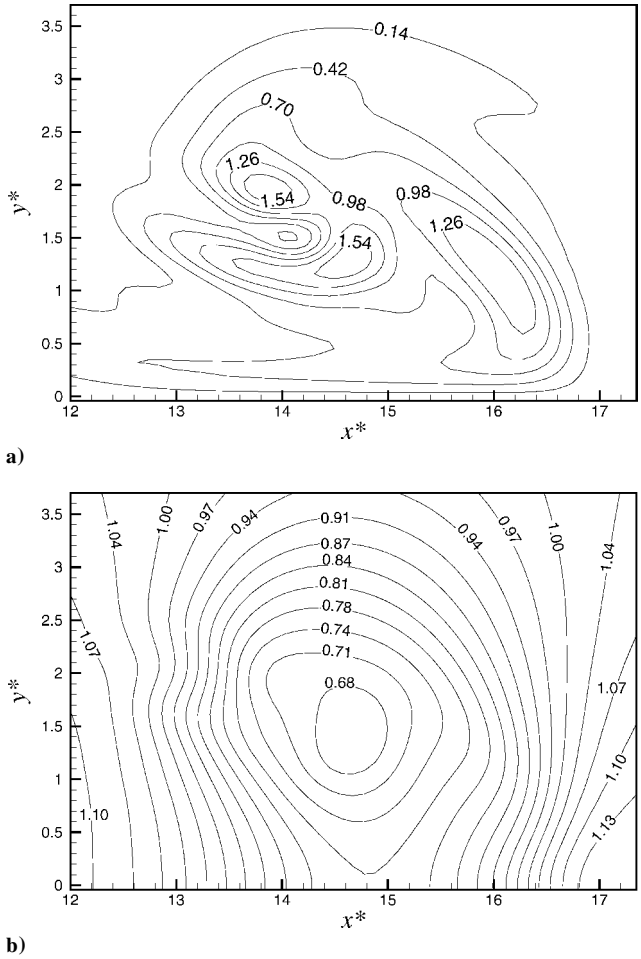

Fig. 14 Closeup of instantaneous a) vorticity and b) pressure contours at $t^* = 48$ for the cavitating case, case D.

between cases A and B. If the vapor pressure is further decreased, eventually a single-phase or noncavitating flow results. Increasing the cavitation number also tends to delay inception and decrease the amplitude of the pressure oscillations as shown in Fig. 13.

C. Effect of Bubble Number Density

The bubble number density is a prespecified constant in Kubota's model. The actual value of this quantity may vary throughout the flow as a result of bubble coalescence and splitting. These effects are not accounted for in the current model. Therefore, it is of interest to examine the effect of this parameter on the interaction between cavitation and vorticity dynamics. In case D, the bubble number density was decreased from 10^6 to 10^4 with all other parameters the same as in case B (Table 1). In Fig. 14, closeups of the vorticity and pressure contours for the same region as in Fig. 9 are shown. Again, the velocity vector plots were similar for both cases and are not shown. The vorticity contours are qualitatively similar to the two preceding cases but are more similar to case B than to case C. One interesting difference is the increase in the peak vorticity in the central vortex. The pressure is lower everywhere than in case B in the region shown. By the lowering of the bubble number density everywhere in the domain, the amount of vapor formed due to cavitation and, hence, the effect on the flow, is less noticeable. If the bubble number density is further decreased, a noncavitating flow is recovered. This can also be seen in the further decrease in the pressure fluctuations as shown in Fig. 15.

D. Effect of Bubble Cluster Radius

The bubble cluster radius Δr is related to the spatial extent over which bubbles may interact with each other dynamically. In case E, the bubble cluster radius is increased from 0.1 to 1.0 with all other parameters the same as in case B. In Fig. 16, the vorticity contours

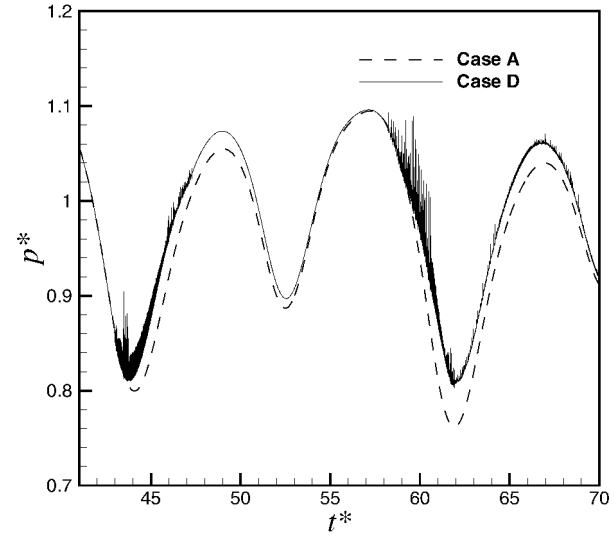

Fig. 15 Temporal evolution of instantaneous pressure at one fixed point for cases A and D.

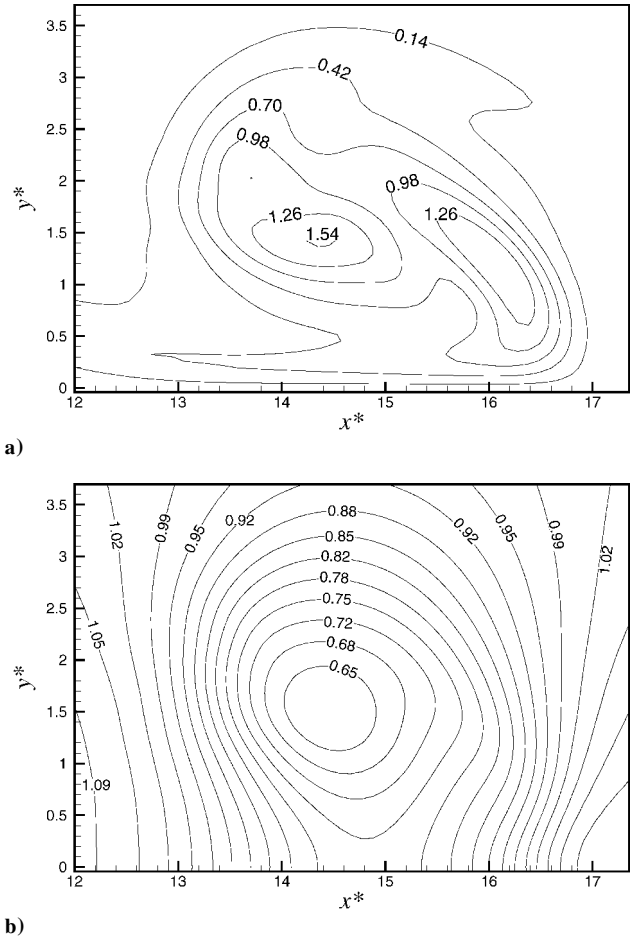

Fig. 16 Closeup of instantaneous a) vorticity and b) pressure contours at $t^* = 48$ for the cavitating case, case E.

reveal only two main vortical structures, most similar to the noncavitating case (case A) but with lower peak values for the vorticity. The pressure is lower everywhere than in case B, but higher than in case A. Increasing the bubble cluster radius increases the amount of diffusion associated with the LHM equation. This damping effect can be revealed in Fig. 17, which shows the temporal evolution of the maximum void fraction for cases B and E. [Note that the corresponding bubble radius evolution can be calculated directly from Eq. (4).] With a smaller bubble cluster radius in case B, the

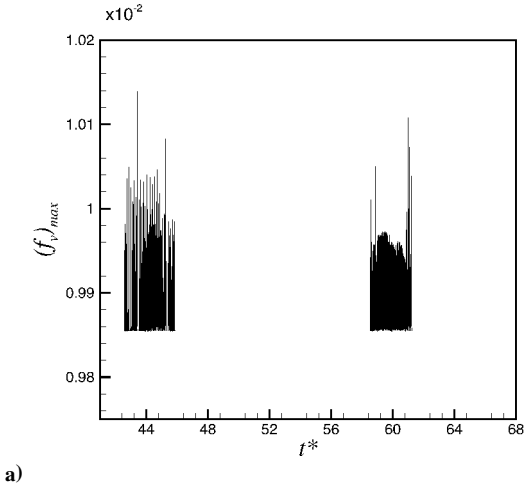

a)

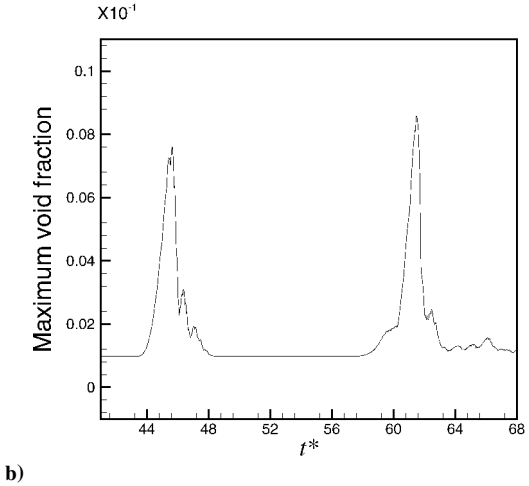

b)

Fig. 17 Temporal evolution of maximum void fraction for a) case B and b) case E.

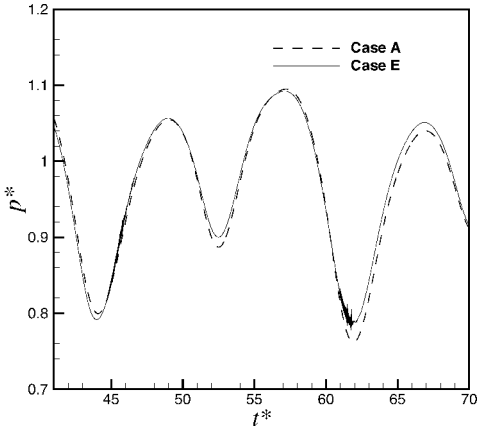

Fig. 18 Temporal evolution of instantaneous pressure at one fixed point for cases A and E.

void fraction increases and decreases with a much higher frequency than that in case E. This is consistent with the recent findings of Delale et al.[11] This damping effect can also be seen in the virtual elimination of pressure fluctuations, as shown in Fig. 18.

E. Vorticity Transport Equation Analysis

To get a better understanding of the effect of cavitation on vorticity dynamics, it is useful to examine the vorticity transport equation for a two-dimensional flow:

$$\frac{\mathrm{D}\omega}{\mathrm{D}t} = -\omega\nabla\cdot\boldsymbol{V} + \frac{\nabla\rho\times\nabla p}{\rho^2} + \nu\nabla^2\omega \qquad (13)$$

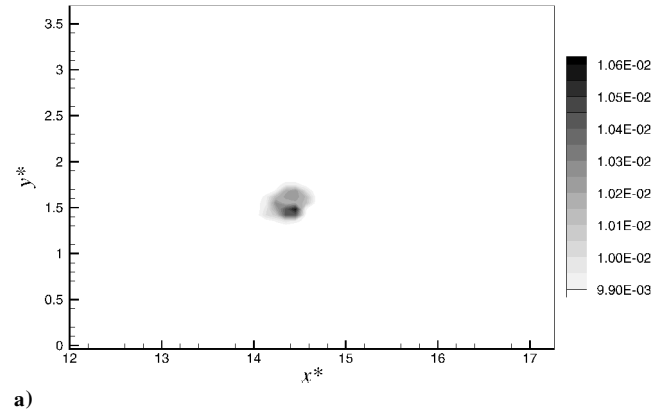

a)

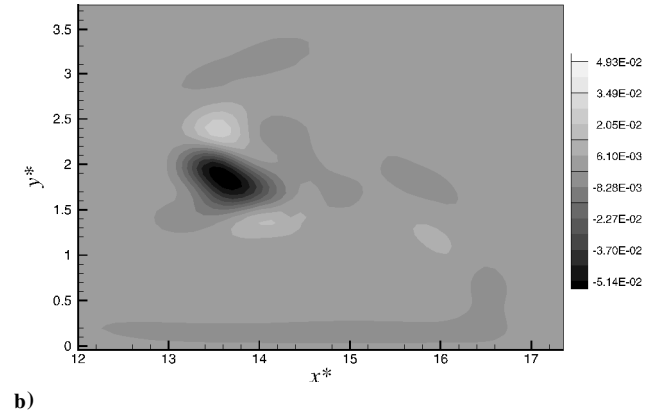

b)

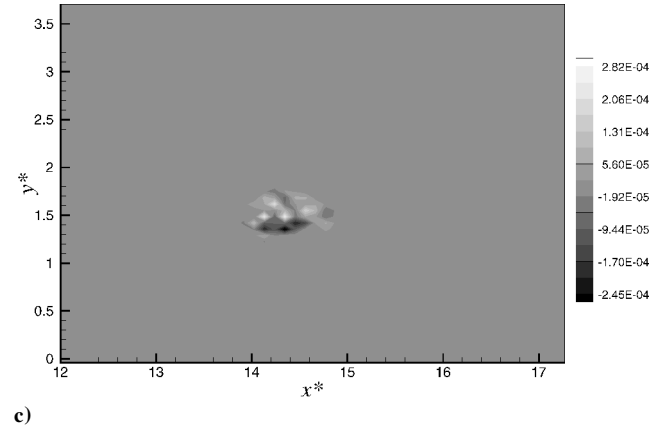

c)

Fig. 19 Closeup of instantaneous a) void fraction, b) dilatation term, and c) baroclinic torque term at $t^* = 48$ for the cavitating case, case E.

The vorticity of a fluid particle can be changed by the various terms on the right-hand side of this equation, which are, from left to right, dilatation, baroclinic torque, and viscous diffusion. Figure 19 shows plots of the instantaneous void fraction (Fig. 19a) along with the dilatation (Fig. 19b) and baroclinic torque (Fig. 19c) terms from the vorticity transport equation. Both the dilatation and the baroclinic torque terms are nonzero in the same general vicinity of the nonzero void fraction region. The baroclinic torque term is more than two orders of magnitude smaller than the dilatation term. Notice that these terms can act as both a source and a sink for vorticity.

F. Effect of Reynolds Number

It has been observed in the experiments of Sridhar and Katz[4] that, for the appropriate number and sizes of bubbles entrained by a vortex, a splitting of the vortex into two separate regions was observed with significant increase in the peak vorticity in each region. To capture this phenomena, results are presented here from case F, a noncavitating case where the Reynolds number was increased

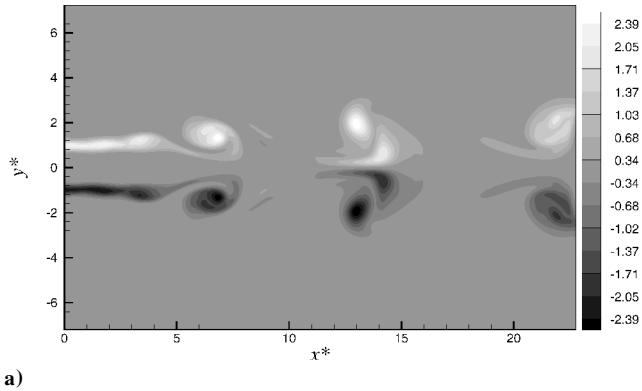

a)

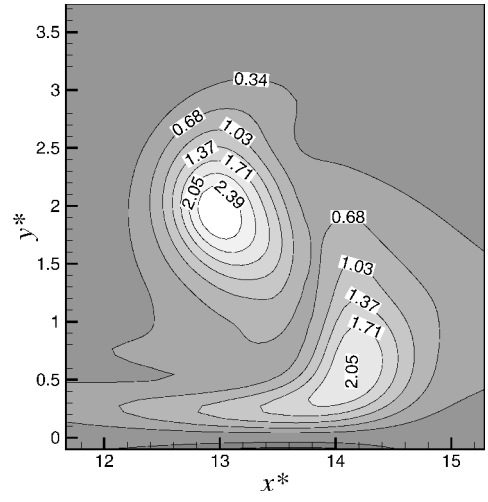

b)

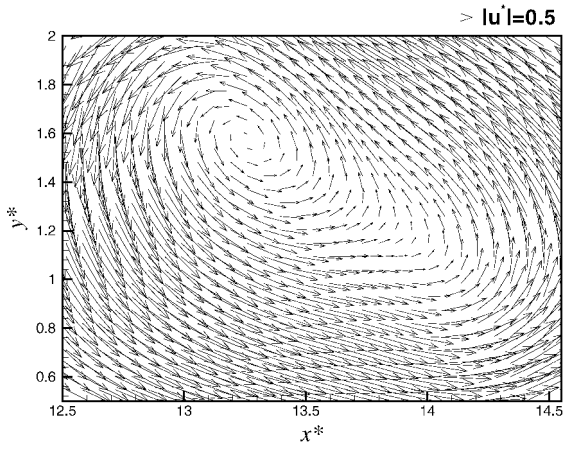

c)

Fig. 20 Instantaneous a) contour plot of vorticity, b) closeup of vorticity, and c) velocity vectors at $t^* = 54$ for noncavitating case, case F.

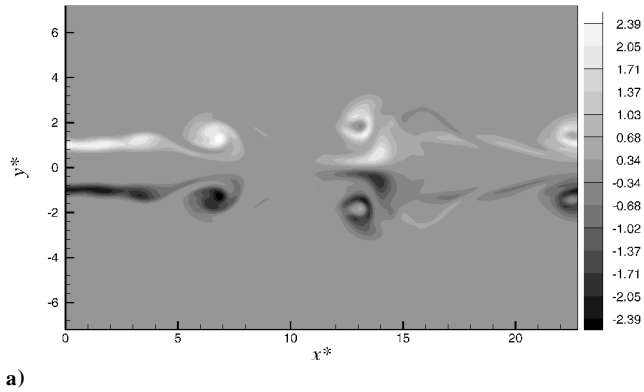

a)

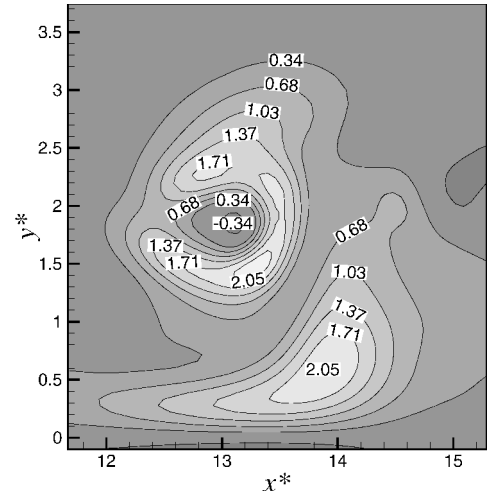

b)

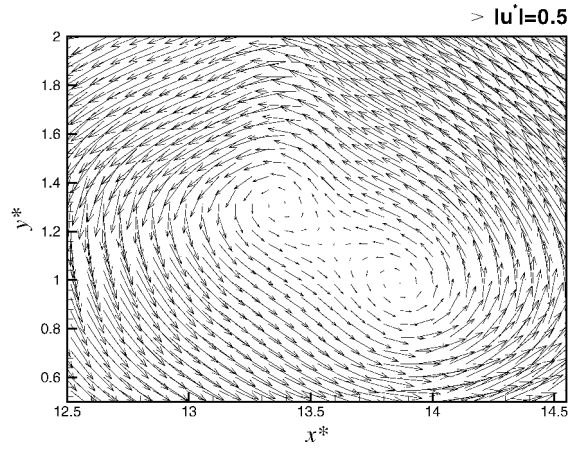

c)

Fig. 21 Instantaneous a) contour plot of vorticity, b) closeup of vorticity, and c) velocity vectors at $t^* = 54$ for cavitating case, case G.

from 6×10^2 to 1×10^3, and from case G, a cavitating case where the Reynolds number was also increased to 1×10^3 and the bubble cluster radius was 0.2. All other parameters were the same as in case B. In Figs. 20c and 21c, closeups of velocity vectors (with $0.6U_0$ subtracted from each vector to highlight the flow pattern) in the region where vapor was present are shown. In the noncavitating case F, a single vortex can be discerned, whereas for the cavitating case G, the vortex has split into two separate vortices with the same sign. This is consistent with previous numerical simulations of Loth et al.[23] The peak vorticity in this region has decreased compared to the noncavitating case. These results suggest that cavitation may inhibit the vortex pairing process, hence stabilizing the jet and affecting the distribution and levels of turbulent kinetic energy. Further experimental measurements and three-dimensional large eddy simulations would be required to investigate this.

VII. Conclusions

Numerical simulations of cavitation in planar submerged laminar jets were conducted. The effects of cavitation and vapor formation on the liquid flow were accounted for in the model. The key flow and cavitation model parameters were varied to study their effect. The processes of vortex rollup and pairing were affected by the presence of vapor associated with the cavitation process. The simulation results were in qualitative agreement with previous experimental studies. Specific findings were as follows:

1) Cavitation occurred in the cores of the vortical structures when the local pressure fell below the vapor pressure.

2) Cavitation suppressed jet growth upstream of the location of the first vortex pairing and enhanced jet growth after the pairing.

3) Cavitation caused the location of the vortex core to shift vertically away from the jet axis.

4) Cavitation inhibited the vortex pairing process.

5) Cavitation tended to distort and elongate the vortical structures.

6) Cavitation set a lower limit for the pressure.

7) Increasing the cavitation number or decreasing the bubble number density weakened the effects of cavitation.

8) Increasing the bubble cluster radius increased damping effects and decreased both the amplitude and frequency of the pressure and void fraction fluctuations.

9) Increasing the Reynolds number with vapor formation at the center of vortex caused the vortex to split into two disjointed vortices with the same sign.

Extensions of the present flow model to three dimensions and inclusion of a subgrid-scale turbulence model will allow large-eddy simulations to be conducted for cavitating jet flows with quantitative comparison to experimental data.

Acknowledgment

The authors would like to acknowledge Caterpillar, Inc., Peoria, Illinois, for their financial support of this research.

References

[1]Arndt, R. E. A., "Cavitation in Fluid Machinery and Hydraulic Structures," *Annual Review of Fluid Mechanics*, Vol. 13, 1981, pp. 273–328.

[2]Rood, E. P., "Review—Mechanisms of Cavitation Inception," *Journal of Fluids Engineering*, Vol. 113, No. 2, 1991, pp. 163–175.

[3]Brennen, C. E., "Phase Change, Nucleation, and Cavitation," *Cavitation and Bubble Dynamics*, Oxford Univ. Press, New York, 1995, pp. 1–33.

[4]Sridhar, G., and Katz, J., "Effect of Entrained Bubbles on the Structure of Vortex Rings," *Journal of Fluid Mechanics*, Vol. 397, 1999, pp. 171–202.

[5]Gopalan, S., Katz, J., and Knio, O., "The Flow Structure in the Near Field of Jets and Its Effects on Cavitation Inception," *Journal of Fluid Mechanics*, Vol. 398, 1999, pp. 1–43.

[6]Cerutti, S., Knio, O. M., and Katz, J., "Numerical Study of Cavitation Inception in the Near Field of an Axisymmetric Jet at High Reynolds Number," *Physics of Fluids*, Vol. 12, No. 10, 2000, pp. 2444–2460.

[7]Rightley, P. M., and Lasheras, J. C., "Bubble Dispersion and Interphase Coupling in a Free-Shear Flow," *Journal of Fluid Mechanics*, Vol. 412, 2000, pp. 21–59.

[8]Turkle, E., "Preconditioning Techniques in Computational Fluid Dynamics," *Annual Review of Fluid Mechanics*, Vol. 31, 1999, pp. 385–416.

[9]Senocak, I., and Shyy, W., "A Pressure-Based Method for Turbulent Cavitating Flow Computations," *Journal of Computational Physics*, Vol. 176, No. 2, 2002, pp. 363–383.

[10]Kubota, A., Kato, H., and Yamaguchi, H., "A New Modelling of Cavitating Flows: A Numerical Study of Unsteady Cavitation on a Hydrofoil Section," *Journal of Fluid Mechanics*, Vol. 240, 1992, pp. 59–96.

[11]Delale, C. F., Schnerr, G. H., and Sauer, J., "Quasi-One-Dimensional Steady-State Cavitating Nozzle Flows," *Journal of Fluid Mechanics*, Vol. 427, 2001, pp. 167–204.

[12]Chen, Y., and Heister, S. D., "Modeling Hydrodynamic Nonequilibrium in Cavitating Flows," *Journal of Fluids Engineering*, Vol. 118, No. 1, 1996, pp. 172–178.

[13]Grogger, H. A., and Alajbegovic, A., "Calculation of the Cavitating Flow in Venturi Geometries Using Two Fluid Model," *Proceedings of the Fluids Engineering Division Summer Meeting*, FEDSM98-5295, American Society of Mechanical Engineers, Fairfield, NJ, 1998, pp. 1–6.

[14]Schmidt, D. P., Rutland, C. J., Corradini, M. L., Roosen, P., and Genge, O., "Cavitation in Two-Dimensional Asymmetric Nozzles," Society of Automotive Engineers, SAE Congress Paper 1999-01-0518, 1999.

[15]Sauer, J., and Schnerr, G. H., "Unsteady Cavitating Flow—A New Cavitation Model Based on a Modified Front Capturing Method and Bubble Dynamics," *2000 ASME Fluids Engineering Division Summer Conference*, FEDSM2000-11095, American Society of Mechanical Engineers, Fairfield, NJ, 2000, pp. 1–7.

[16]Kanno, T., Aoki, T., Takahashi, K., and Nonoshita, T., "Study of Flow in a Spool Valve," *Individual Papers in Fluids Engineering*, FED-Vol. 207, American Society of Mechanical Engineers, Fairfield, NJ, 1995, pp. 87–92.

[17]Lele, S. K., "Compact Finite Difference Schemes with Spectral-Like Resolution," *Journal of Computational Physics*, Vol. 103, No. 1, 1992, pp. 16–42.

[18]Briggs, W. L., "Elements of Multigrid," *A Multigrid Tutorial*, Society for Industrial and Applied Mathematics, Philadelphia, 1987, pp. 33–50.

[19]Liu, C., and Liu, Z., "Multigrid Methods and High–Order Finite Difference for Flow in Transition," *11th AIAA Computational Fluid Dynamics Conference*, AIAA, Washington, DC, 1993, pp. 615–641.

[20]Akaike, S., and Nemoto, M., "Potential Core of Submerged Laminar Jet," *Jets and Cavities—International Symposium*, FED-Vol. 31, American Society of Mechanical Engineers, Fairfield, NJ, 1985, pp. 85–92.

[21]Druzhinin, O. A., and Elghobashi, S. E., "Direct Numerical Simulation of a Three-dimensional Spatially Developing Bubble-Laden Mixing Layer with Two-Way Coupling," *Journal of Fluid Mechanics*, Vol. 429, 2001, pp. 23–61.

[22]Kjeldsen, M., Arndt, R. E. A., and Effertz, M., "Spectral Characteristics of Sheet/Cloud Cavitation," *Journal of Fluids Engineering*, Vol. 122, No. 3, 2000, pp. 481–487.

[23]Loth, E., Boris, J. P., and Emery, M., "Very Large Bubble Cavitation in a Temporally-Evolving Free Shear Layer," *1998 ASME Fluids Engineering Division Summer Meeting*, FEDSM98-5028, American Society of Mechanical Engineers, Fairfield, NJ, 1998, pp. 1–8.

J. R. Bellan
Associate Editor